Stability analysis and design of time-domain acoustic impedance boundary conditions for lined duct with mean flow

Xin Liu
State Key Laboratory of Turbulence and Complex Systems, College of Engineering, Peking University, Beijing 100871, China

Xun Huang[a)]
Department of Aeronautics and Astronautics, College of Engineering, Peking University, Beijing 100871, China

Xin Zhang
Airbus Noise Technology Center, Faculty of Engineering and the Environment, University of Southampton, Highfield, Southampton SO17 1BJ, United Kingdom

(Received 11 June 2014; revised 20 August 2014; accepted 18 September 2014)

This work develops the so-called compensated impedance boundary conditions that enable stable time domain simulations of sound propagation in a lined duct with uniform mean flow, which has important practical interest for noise emission by aero-engines. The proposed method is developed analytically from an unusual perspective of control that shows impedance boundary conditions act as closed-loop feedbacks to an overall duct acoustic system. It turns out that those numerical instabilities of time domain simulations are caused by deficient phase margins of the corresponding control-oriented model. A particular instability of very low frequencies in the presence of steady uniform background mean flow, in addition to the well known high frequency numerical instabilities at the grid size, can be identified using this analysis approach. Stable time domain impedance boundary conditions can be formulated by including appropriate phaselead compensators to achieve desired phase margins. The compensated impedance boundary conditions can be simply designed with no empirical parameter, straightforwardly integrated with ordinary linear acoustic models, and efficiently calculated with no need of resolving sheared boundary layers. The proposed boundary conditions are validated by comparing against asymptotic solutions of spinning modal sound propagation in a duct with a hard-soft interface and reasonable agreement is achieved.
 [http://dx.doi.org/10.1121/1.4896746]

PACS number(s): 43.28.Py, 43.28.En [AH] Pages: 2441–2452

I. INTRODUCTION

Acoustic liners are usually used on aero-engine nacelles and in ducts to reduce fan noise emission[1,2] that has attracted continued practical interest to meet increasingly stringent regulations in terms of environment consideration. A simple acoustic liner consists of a perforated facing sheet and enclosed cavities.[3] The associated bulk property is an acoustic impedance that is usually defined in the frequency domain as the ratio of the local sound pressure and the normal particle velocity (pointing into the surface). Optimizations of liner applications request effective numerical simulation methods. Time domain solvers based on linearized Euler equations (LEE)[4] gradually become popular for noise predictions within lined ducts.[5–7] One of the most difficult and key issues for a time domain solver is lining impedance boundary conditions, which usually lead to numerical instabilities and have therefore received prime attention in recent studies.[5,8,9] The objective of this work is to propose a new analysis method and design strategy for time domain impedance boundary conditions.

Numerical instabilities could arise in time domain simulations of duct acoustic propagations for various reasons. First, the LEE model not only describes sound wave propagation but also permits vortical wave development[10] that would grow in sheared flows[11,12] grazing on lined surfaces. This shear layer issue can be resolved if the Ingard-Myers boundary conditions[13,14] are used by assuming a vanishingly thin boundary layer.[15] However, recent work shows that Ingard-Myers boundary conditions are ill-posed[8,16] and would induce absolute instability for uniformly grazing flows. A couple of modified Ingard-Myers boundary conditions have been proposed mainly from a theoretical perspective[9,17,18] to capture the previously overlooked fluid dynamics. In particular, an empirical parameter has been proposed into a liner model[17] to represent fluid momentum transfer. A more generally accepted treatment developed by Brambley[9] and by Rienstra and Darau[18] takes account of boundary layer profiles of finite thickness in the modified Ingard-Myers boundary conditions, whose performance has been numerically examined by Gabard[19] in a canonical test case of plane wave reflection.

Second, the impedance of a liner is usually given in the frequency domain as $Z(s)$, where s is complex argument associated with Laplace transform. Nevertheless, the

a)Author to whom correspondence should be addressed. Electronic mail: huangxun@pku.edu.cn

corresponding time domain implementation might violate causality.[8] Tam and Auriault[20] proposed a causal time domain impedance boundary condition for stationary mean flow, by using a fascinated analysis of mathematical mapping. This boundary condition was then extended by Li *et al.*[21] to subsonic flow cases. The issue of numerical instabilities, however, still remained unresolved. On the other hand, Özyörük and Long constructed stable numerical implementations of a given $Z(s)$ using Z-transform,[22] which is the discrete-time equivalent of the Laplace transform, usually used in digital control or digital signal processing. The essential concept is to asymptotically represent $Z(s)$ in the z-plane with all poles within the unit circle that ensures bounded input bounded output (BIBO) stability.[23] The success of this method would highly depend on the empirically asymptotic representation. In addition, Fung and Ju have developed a series of time domain impedance boundary conditions without any empirical parameter,[24–26] by replacing impedance with its corresponding reflection coefficient. The whole manipulation is very skillful and actually (implicitly) adopts the BIBO stability concept. More specifically, the reflection coefficient is actually a bilinear transformation of $-Z(s)$. Then, all poles of the reflection coefficient would reside inside the unit circle in the transformed z-plane since $-\mathrm{Re}(Z(s)) < 0$ for passive liners.

The computational cost of the modified Ingard-Myers would be extensively increased to resolve sound propagations within boundary layer profiles, not to mention the unavailability of boundary layer profiles for many practical problems. In numerical implementations, the boundary conditions proposed by Fung and Ju are quite generic and stable over various flow conditions. However, the associated LEE model has to be reconstructed specifically for incident waves and reflected waves. This work is motivated by the fact that an efficient impedance boundary condition of $Z(s)$ for the ordinary LEE model with a uniform flow is still lacked. We will propose new boundary conditions directly from the very unusual perspective of feedback control that enables efficient stability analysis rather than using the rigorous Briggs-Bers criterion, which seemed to be impractical for cylindrical duct cases.[16] Then, the design of stable impedance boundary conditions can be regarded as a control design problem, which is hopefully simple to conduct and easy to integrate with the ordinary LEE model. It should be noted that almost all previous work has been numerically validated only using the most simple plane wave cases.[9,19,22,24–26] Spinning modal sound propagation through a lined duct has been numerically studied by Richter *et al.*[27] and by Özyörük and Ahuja[28] but without any verification and validation. In this work, we will validate the proposed impedance boundary conditions by comparing to analytical solutions of spinning modal sound propagations through lined duct cases with hard-soft wall interfaces.

The remaining part of this paper is organized as follows. Section II introduces the ordinary LEE model, computational set-ups and numerical instability issues. The developing of the new impedance boundary conditions requests a control-oriented model, which is developed from the LEE model and the detailed derivation is given in Sec. III. Then, a stability analysis is performed in Sec. IV to show the deficiency of some classical time domain impedance boundary conditions. As a remedy, the proposed stable impedance boundary conditions are designed in Sec. V using the proposed feedback control design strategy. Numerical simulations are conducted in Sec. VI to validate the proposed boundary conditions by comparing against asymptotic solutions using the Wiener-Hopf method,.[8,29–31] Finally, Sec. VII summarizes the present work.

II. STATEMENT OF THE PROBLEM

A. Governing equations

The governing equations for this work are developed from the Euler equations for an inviscid compressible perfect gas,

$$\frac{\partial \rho}{\partial t} + \nabla \cdot (\rho \mathbf{u}) = 0, \quad \rho \frac{\mathrm{D}\mathbf{u}}{\mathrm{D}t} = -\nabla p, \quad \frac{\mathrm{D}p}{\mathrm{D}t} = \frac{\gamma p}{\rho}\frac{\mathrm{D}\rho}{\mathrm{D}t}, \tag{1}$$

where ρ is the density, p the pressure, γ the ratio of specific heat, $\mathbf{u} = (u, v, w)$ the velocity, t the sound wave propagation time, and $\mathrm{D}/\mathrm{D}t = \partial/\partial t + \mathbf{u} \cdot \nabla$. It should be noted that this work adopts cylindrical coordinates, where $\partial \cdot \mathbf{u} = \partial u/\partial x + \partial v/\partial r + 1/r(\partial w/\partial \theta)$, with x as the axial coordinate, r as the radial coordinate, and θ as the circumferential angle.

In acoustic simulations, we assume both the time scale and length scale of fluid dynamics to be much larger than the scales of spinning sound waves. Then, we decompose the flow field as

$$\rho = \rho_0 + \rho', \quad p = p_0 + p', \quad \mathbf{u} = \mathbf{u}_0 + \mathbf{u}', \tag{2}$$

where the subscript $(\cdot)_0$ denotes the mean flow fluid and the superscript $(\cdot)'$ represents acoustic waves. This decomposition enables the use of LEE as the computational model to describe sound propagations through a steady, incompressible background flow. To further reduce the expensive computational cost of the full 3D LEE model, here we adopt the so-called 2.5D LEE model proposed by Zhang *et al.*,[32] which would simplify the general 3D LEE model to a set of 2D equations for an incident spinning modal wave at the tonal frequency ω_0 and circumferential mode m,

$$\frac{\partial u'}{\partial t} + M_0 \frac{\partial u'}{\partial x} + \frac{\partial p'}{\rho_0 \partial x} = 0, \tag{3a}$$

$$\frac{\partial v'}{\partial t} + M_0 \frac{\partial v'}{\partial x} + \frac{\partial p'}{\rho_0 \partial r} = 0, \tag{3b}$$

$$\frac{\partial \dot{w}'}{\partial t} + M_0 \frac{\partial \dot{w}'}{\partial x} + \frac{m\omega}{\rho_0 r} p' = 0, \tag{3c}$$

$$\frac{\partial p'}{\partial t} + M_0 \frac{\partial p'}{\partial x} + \rho_0 \frac{\partial u'}{\partial x} + \rho_0 \frac{\partial v'}{\partial r} - \frac{m\rho_0}{\omega r}\dot{w}' + \frac{\rho_0 v'}{r} = 0, \tag{3d}$$

where $\dot{w}' \triangleq \partial w'/\partial t$. With little loss of generality, the background mean flow is parallel to the axial axis, i.e., $\mathbf{u}_0 = (M_0, 0, 0)$. In addition, the fluid is modeled as a perfect gas with the homentropic assumption, i.e., $\rho' = c_0^2 \rho'$, where

c_0 is the speed of sound. It should be noted that all variables are non-dimensionalized using a reference length L^*, a reference speed c_0^*, and a reference density ρ^*. For the numerical examples considered in this work, these references have been taken as 1 m, 340 m/s, and 1.225 kg/m^3. In addition, it is worthwhile to mention that the maximal value of the normalized M_0 (i.e., the flow Mach number) is 0.3. Otherwise, the incompressible assumption used in this LEE model would be inappropriate. More details of the 2.5D LEE model can be found in Refs. 6, 32, and 33.

B. Computational set-up and numerical instability

The computational set-up is shown in Fig. 1, which is the most simplified case of a lined bypass duct. A slip-wall boundary condition is used for the hard wall at $r = 1$ and $x < 0$. A liner is installed on the inner wall of the cylindrical duct at $r = 1$ and $x \geq 0$. The lined wall is usually regarded as a soft surface and the hard-soft interface is thus at $x = 0$, $r = 1$. The sound field is calculated using the in-house acoustic code[11] with fourth-order low-dispersion and low-dissipation computational methods.[34–36] A tenth-order filter is used throughout the computational grids to remove spurious numerical waves developing during the computation.[34] A single-side tenth-order filter[37] is performed at the grid points local to and on the lined wall. The resolution of the computational mesh ensures at least 10 points-per-wavelength.[10,36]

For the sake of generality and simplicity, here we consider the incident sound wave of the tonal frequency ω_0 with a single circumferential mode m and a single radial mode n from upstream. A further simulation of a broadband sound wave with multiple modes will require linear superposition. The buffer zone technology[38] is adopted at the upstream and downstream boundaries. The target solution of the (right) outlet buffer zone is set to zero so that it absorbs spurious reflection and simulates far-field conditions. The target solution of the (left) inlet buffer zone is set to be an incident spinning modal sound wave that allows incident wave into the computational domain. For the idealized geometry with a straight infinite and hard walled duct, Eqs. (3a)–(3d) have analytical solutions for the mth azimuthal mode at a single frequency ω_0 as follows:

$$p'_m(x,r,\theta,t) = \mathrm{Re}[A_{ac}\mathrm{J}_m(\alpha_{mn}r)\exp(i\omega_0 t - i\kappa_{mn}^{+}x - im\theta)], \tag{4a}$$

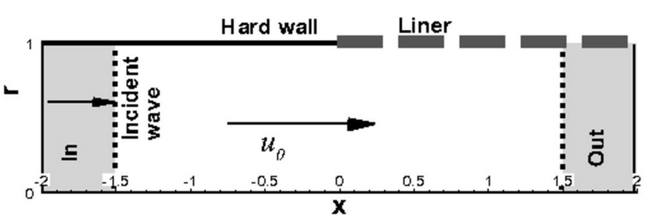

FIG. 1. The computational set-up of the numerical acoustic simulations (not to scale) for duct acoustics. A spinning modal sound wave will be incident from left to right. Buffer zones (the two grayed regions) are used at the upstream and downstream sections. The boundary conditions are set to axial-symmetrical at $r = 0$, hard wall at $r = 1$ and $x < 0$, and lined wall at $r = 1$ and $x > 0$, respectively. The circumferential angle θ is not shown here.

$$u'_m(x,r,\theta,t) = \mathrm{Re}\left[A_{ac}\frac{\kappa_{mn}^{+}}{\omega_0 - M_0\kappa_{mn}^{+}}\mathrm{J}_m(\alpha_{mn}r)\right. \\ \left.\times\exp\left(i\omega_0 t - i\kappa_{mn}^{+}x - im\theta\right)\right], \tag{4b}$$

$$v'_m(x,r,\theta,t) = \mathrm{Re}\left[iA_{ac}\frac{\alpha_{mn}}{\omega_0 - M_0\kappa_{mn}^{+}}\dot{\mathrm{J}}_m(\alpha_{mn}r)\right. \\ \left.\times\exp\left(i\omega_0 t - i\kappa_{mn}^{+}x - im\theta\right)\right], \tag{4c}$$

$$w'_m(x,r,\theta,t) = \mathrm{Re}\left[A_{ac}\frac{m}{r(\omega_0 - M_0\alpha_{mn})}\mathrm{J}_m(\alpha_{mn}r)\right. \\ \left.\times\exp\left(i\omega_0 t - i\kappa_{mn}^{+}x - im\theta\right)\right], \tag{4d}$$

where A_{ac} is the amplitude of the acoustic perturbation (here its non-dimensional value is set to 10^{-4}), J_m the mth-order Bessel function of the first kind, $i = \sqrt{-1}$, and $\dot{\mathrm{J}}_m \triangleq \mathrm{dJ}_m/\mathrm{d}r$. For an incident wave developing from a hard wall, the nth radial wave number α_{mn} of the mth spinning mode is the nth solution of the following equation determined by the hard-wall boundary condition of the duct,

$$\frac{\mathrm{d}[Jm(\alpha_{mn}R)]}{\mathrm{d}r} = 0, \tag{5}$$

where R is the radius of the outer duct wall and its normalized value is set to unit. The axial wave number in the x axis can be subsequently calculated using

$$\kappa_{mn}^{\pm} = \frac{\omega}{1 - M_0^2}\left(-M_0 \pm \sqrt{1 - \frac{\alpha_{mn}^2\left(1 - M_0^2\right)}{\omega^2}}\right), \tag{6}$$

where κ_{mn}^{+} corresponds to the downstream-propagating incident wave and κ_{mn}^{-} corresponds to the upstream-directed spinning wave. In this work, only the right-propagating wave with κ_{mn}^{+} is used in the inlet buffer zone.

C. Impedance boundary conditions

The impedance of a locally reactive liner is usually defined in frequency domain as the ratio of sound pressure and the normal velocity pointing into the local lining surface, i.e., $Z(s) = \hat{p}'(s)/\hat{v}'(s)$, for duct cases with a stationary flow. To be consistent with the following text, here we use Laplace transform, e.g., $\hat{p'}(s) = \int_0^{+\infty} p'(t)\exp(-st)dt$, instead of the Fourier transform usually adopted in the definition of the impedance boundary conditions. In this work, our attention is primarily focused on spinning modal sound propagations within a straight duct at a tonal frequency of ω_0, with the impedance of $Z(s)|_{s=i\omega,\omega=\omega_0} = \Re + i\mathfrak{X}$, where $(\Re,\ \mathfrak{X})$ are real, $\Re > 0$ for passive liners.

Acoustic solutions of lined wall cases take the same form as Eqs. (4a)–(4d). The relation between the axial wave number and the radial wave number, Eq. (6), also remains applicable, whereas the hard wall boundary condition of Eq. (5) should be replaced by

$$(i\omega - iM_0\kappa_{mn}^{\pm})\hat{p}'_m(x,r,\theta,\omega) = i\omega\hat{v}'_m(x,r,\theta,\omega)Z(\omega), \quad (7)$$

which is a variant form of the Ingard boundary condition. If $p'_m(x,r,\theta,t)$ and $v'_m(x,r,\theta,t)$ are represented by Eq. (4a) and Eq. (4c), respectively, from Eq. (7), we will have

$$\left[-i\omega Z(\omega) + \frac{\left(\omega - M_0\kappa_{mn}^{\pm}\right)^2 \mathrm{J}_m(\alpha_{mn}R)}{\alpha_{mn}\mathrm{J}'_m(\alpha_{mn}R)}\right] = 0. \quad (8)$$

Then, $\kappa_{mn}^{\pm}$ is found by solving Eq. (6) and Eq. (8) together. As an example, Fig. 2 shows the trajectories of $\kappa_{mn}^{\pm}$ for the case with $m=4$, $\omega_0 = 10$, $n=1$ to 3, where $\Re \triangleq \mathrm{Re}(Z)$ is set to 1.0, M_0 set to 0.3 and $\mathfrak{X} \triangleq \mathrm{Im}(Z)$ varying from $-\infty$ to $+\infty$. Figure 2 shows that $\mathrm{Im}(\kappa_{mn}^{+}) \neq 0$ for a lined duct, suggesting that the axial acoustic power would be absorbed by liners.

It should be noted that the above analysis takes no account of hard-soft interfaces and is free of numerical instabilities. In contrast, a direct implementation of $Z(s)|_{s=i\omega,\omega=\omega_0} = \Re + i\mathfrak{X}$ in a time domain solver usually leads to numerical instabilities. Here we propose a couple of new impedance boundary conditions, first for simple cases with stationary background flow [at $M_0 = 0$)], as follows:

$$\frac{\hat{v}'(s)}{\hat{p}'(s)} = \frac{1}{Z(s)} = \begin{cases} s/(\Re s - \mathfrak{X}\omega_0), & \text{if } \mathfrak{X} \le 0, \\ L_a(s)\cdot\omega_0/(\Re\omega_0 + \mathfrak{X}s), & \text{if } \mathfrak{X} > 0, \end{cases} \quad (9)$$

with

$$L_a(s) = \frac{1 + aT_a s}{1 + T_a s}\frac{1}{A_{pl}}, \quad \frac{1}{aT_a} = \omega_0, \quad \frac{1}{T_a} = \omega_{\max},$$
$$A_{pl} = \sqrt{\frac{1 + (aT_a\omega_0)^2}{1 + (T_a\omega_0)^2}}, \quad (10)$$

where ω_{max} represents the maximum angular frequency that would be resolvable in the adopted numerical solver, i.e.,

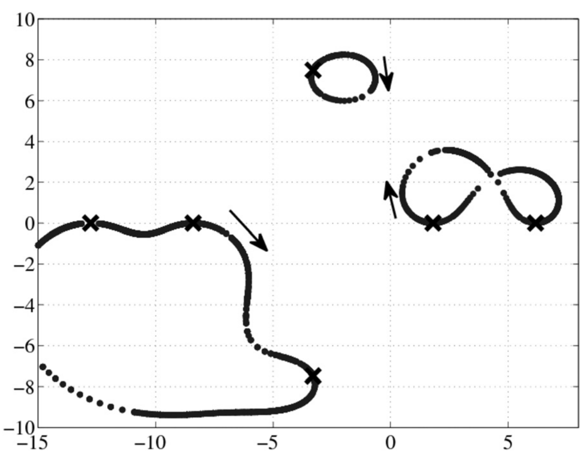

FIG. 2. Trajectories of $\kappa_{mn}^{\pm}$ for $\mathfrak{X}$ varying from $-\infty$ to $+\infty$, where $m=4$, $\omega_0 = 10$, $\Re = 1$, and $M_0 = 0.3$. The symbol $\times$ in this figure represents $\kappa_{mn}^{\pm}$ for the hard wall case with $n=1$ to 3.

$\omega_{max} = 2\pi/\Delta t$, Δt is the associated time advancing step of the solver. Here, the boundary condition is deliberately represented as $1/Z$ that will facilitate the stability analysis conducted in the following section. The corresponding time domain impedance boundary conditions are

$$\text{if } \mathfrak{X} \le 0, \quad \Re\frac{\partial v'}{\partial t} = \frac{\partial p'}{\partial t} + \mathfrak{X}\omega_0 v', \quad (11)$$

if $\mathfrak{X} > 0$,

$$\mathfrak{X}T_a\frac{\partial v'}{\partial t} = \frac{\omega_0\int_0^t p'dt + aT_a\omega_0 p'}{A_{pl}} - \left(\omega_0\Re\int_0^t v'dt + T_a\omega_0\Re v' + \mathfrak{X}v'\right), \quad (12)$$

where the properties of Laplace transform, $s \leftrightarrow \partial/\partial t$ and $1/s \leftrightarrow \int_0^t$, between frequency domain and time domain are adopted.

If the mean flow is steady uniform ($M_0 \neq 0$), the impedance of a straight lined wall is usually defined by the Ingard boundary condition[13]

$$\left(s + M_0\frac{\partial}{\partial x}\right)\hat{p}'(s) = s\hat{v}'(s)Z(s), \quad (13)$$

where the background flow is presumably uniform and slipping at the lining boundary. Eversman and Beckemeyer[15] have proved that sound propagation within a duct with a vanishingly thin shear layer converges to the case with a uniform flow. Recently, it became well-accepted that the Ingard boundary condition and its extended version, the Myers boundary condition,[14] are ill-posed[16] and would induce absolute instability.[8] Brambley[9] and Rienstra and Darau[18] have developed modified Ingard-Myers boundary conditions for an inviscid boundary layer with a finite thickness. However, according to our best knowledge, a successful demonstration of these so-called well-posed boundary conditions in time-domain duct simulations is still not available.

Here we propose a stable version of Ingard boundary condition for steady uniform background flow case ($M_0 \neq 0$ and $M_0 < 0.3$),

$$\frac{\hat{v}'(s)}{\hat{p}'(s)} = \frac{1}{Z(s)} = \begin{cases} I_g(s)\cdot L_b(s)\cdot s/(\Re s - \mathfrak{X}\omega_0), & \text{if } \mathfrak{X} \le 0, \\ I_g(s)\cdot L_b(s)\cdot L_a(s)\cdot\omega_0/(\Re\omega_0 + \mathfrak{X}s), & \text{if } \mathfrak{X} > 0, \end{cases} \quad (14)$$

with

$$I_g(s) = \frac{s + M_0\partial/\partial x}{s}, \quad L_b(s) = \left(\frac{T_b s}{T_b s + 1}\right)^b, \quad (15)$$

where $b=2$, $T_b = 1$, and $L_a(s)$ is the same as that in Eq. (9). The corresponding implementation of time domain impedance boundary conditions are if $\mathfrak{X} \le 0$,

$$\left(-\Re + \omega_0^2\Re + 2\omega_0\mathfrak{X}\right)\frac{\partial v'}{\partial t} = \omega_0^2\frac{\partial p'}{\partial t} + M_0\omega_0^2\frac{\partial p'}{\partial x} - \omega_0\mathfrak{X}v' - 2\Re\omega_0^2 v' + \omega_0^3\mathfrak{X}v', \tag{16}$$

if $\mathfrak{X} > 0$,

$$\begin{aligned}&\left(\mathfrak{X}\text{–}\mathfrak{X}\omega_0^2 + 2\omega_0\Re - 2T_a\mathfrak{X}\omega_0^2 - \omega_0^3\Re T_a + \omega_0\Re T_a\right)\frac{\partial v'}{\partial t}\\ &= -\omega_0^3 p' + M_0\omega_0\frac{\partial}{\partial x}\left(\frac{\partial p'}{\partial t}\right) - \omega_0^3 T_a A_{pl}\frac{\partial p'}{\partial t}\\ &\quad - M_0 T_a A_{pl}\omega_0^3\frac{\partial p'}{\partial x} - \omega_0\Re v' + 2\omega_0^2\mathfrak{X}v'\\ &\quad + \omega_0^3\Re v' + T_a\mathfrak{X}\omega_0^2 v' - T_a\mathfrak{X}\omega_0^4 v' + 2\omega_0^3\Re T_a v'.\end{aligned} \tag{17}$$

It should be emphasized that Eqs. (9)–(17) are the main contribution of this paper. The developments are given in the following sections.

III. NEW PERSPECTIVE FROM CONTROL

A. Control-oriented model

The proposed impedance boundary conditions are developed from the perspective of control. First, a control-oriented model that describes spinning modal sound propagation should be developed. In other words, the LEE model [Eqs. (3a)–(3d)] should be reformulated to the following canonical form in control,

$$\frac{\mathrm{d}}{\mathrm{dt}}\mathbf{x}(t) = \mathbf{Ax} + \mathbf{Bu}, \quad \mathbf{y} = \mathbf{Cx}, \tag{18}$$

where $\mathbf{x}$ and $\mathbf{u}$ represent internal states and inputs of the model; $\mathbf{y}$ denotes model outputs; and $\mathbf{A}$, $\mathbf{B}$, and $\mathbf{C}$ are dynamic, control, and output matrices, respectively. After applying the Laplace transform, the resultant transfer function (i.e., the ratio of an output and an input) of the system is $P(s) = \mathbf{C}(S\mathbf{I} - \mathbf{A})^{-1}\mathbf{B}$. In this work, x represents acoustic quantities, which are functions of time t and spatial coordinates (x, r, θ). We concern ourselves with the system model only on the impedance boundaries at $r = 1$ because almost all instabilities are initially developed therein.

Explicit representation of spatial boundary conditions is one of the most difficult issues in control-oriented modeling. In this work, we apply the concept of generalized function and consider lining impedance boundary conditions at $r = 1$ with discontinuous normal particle velocity (v'). Then, the generalized spatial derivative in r axis is

$$\left.\frac{\bar{\partial} v'(t,r)}{\partial r}\right|_{r=1} = \left.\frac{\partial v'(t,r)}{\partial r}\right|_{r=1} + \left[v'(t,r)|_{r=1^+} - v'(t,r)|_{r=1^-}\right]\cdot\delta(r-1), \tag{19}$$

where $\bar{\partial}/\partial r$ denotes a generalized derivative and δ is Dirac delta function. The numerical manipulation of $\delta(r-1)$ can be found in Ref. 39. Applying the Laplace transform, we would have

$$\left.\frac{\bar{\partial}\hat{v}'(s,r)}{\partial r}\right|_{r=1} = \left.\frac{\partial \hat{v}'(s,r)}{\partial r}\right|_{\mathrm{r}=1} + \left[\hat{v}'(s,r)|_{\mathrm{r}=1^+} - \hat{v}'(s,r)|_{\mathrm{r}=1^-}\right]\cdot\delta(r-1). \tag{20}$$

Suppose $v'(r)|_{r=1^+} = 0$ and then $\hat{v}'|_{r=1^+} = 0$, Eq. (3d) in the LEE model becomes

$$s\hat{p}' + M_0\frac{\partial\hat{p}'}{\partial x} + \frac{\partial\hat{u}'}{\partial x} + \frac{\bar{\partial}\hat{v}'}{\partial r} - \frac{m}{\omega}\hat{w}' + \frac{\hat{v}'}{r} = \underbrace{-\hat{v}'|_{r=1^-}\cdot\delta(r-1)}_{\text{The negative feedback!}} \tag{21}$$

at $r = 1$, where the subscript $(\cdot)|_{r=1}$ is omitted for most variables for clarity. The right-hand side term shows a negative feedback to the original LEE model due to lining surfaces, which is one of the most important findings in this work. Figure 3(a) shows the entire feedback system, where the system input e represents potential physical disturbances, numerical, and modeling errors.

The next step is to simplify the spatial derivatives in Eq. (21). First, the generalized derivative $\bar{\partial}/\partial r$ can be simply approximated by using single-side computational stencils, such as $\bar{\partial}(\cdot)/\partial r|_{r=1} \approx [(\cdot)_{r=1} - (\cdot)_{r=1-\Delta r}]/\Delta r$, with Δr the axial discretization step. Second, a sound wave would scatter during its passage through a discontinuous hard-soft interface. An initial single circumferential modal sound field of mode (m, n) will develop to

$$p'(x,r,\theta,t) = \sum_{l=0}^{+\infty}[A_{ml}^+\exp(-i\kappa_{ml}^+ x) + A_{mn}^- \times \exp(-i\kappa_{ml}^- x)]\mathrm{J}_m(\alpha_{ml}r)\exp(i\omega t - im\theta). \tag{22}$$

In other words, the resultant sound field would have the same circumferential mode m but with various radial modes n. Here we assume that the original mode, (m, n), is still dominant in the overall sound field, i.e., $p'(x,r,\theta,t) \approx A_{mn}^+\exp(-i\kappa_{mn}^+ x) \times \mathrm{J}_m(\alpha_{mn}r)\exp(i\omega t - im\theta)$. Then, $\partial\hat{p}'/\partial x \approx -i\kappa_{mn}^+\hat{p}'$, and

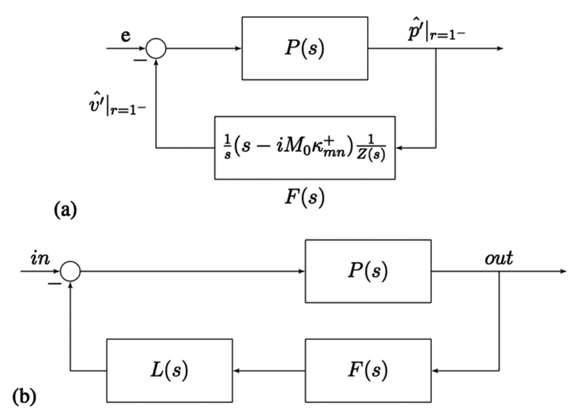

FIG. 3. The block diagram of feedback systems. (a) A description of the LEE model at $r = 1$ [the feed-forward loop, $P(s)$ with a lined wall satisfying the Ingard boundary condition [the feedback loop, $F(s)$]; and (b) an additional phase-lead compensator, $L(s)$, is included in the feedback loop that would stabilize the entire system. The derivation of $F(s) = (s - iM_0\kappa_{mn}^+)/(sZ(s))$ can be found in Sec. IV C. For clarity, $\delta(r-1)$ is not shown in the figure.

Eq. (13) would be simplified to $sZ(s)\hat{v}'(s,r)|_{r=1-} \approx (s - iM_0\kappa_{mn}^+)\hat{p}'(s,r)|_{r=1-}$, which is Eq. (7) if $s = i\omega$.

Finally, we simplify the original LEE model [Eqs. (3a)–(3d)] on the lined wall at $r = 1$ and $x \geq 0$ to the following canonical form in control

$$\underbrace{\frac{\mathrm{d}}{\mathrm{d}t}\begin{bmatrix} u'|_{r=1} \\ v'|_{r=1} \\ w'_t|_{r=1} \\ p'|_{r=1} \end{bmatrix}}_{\mathrm{dx/dt}} = \underbrace{\begin{bmatrix} i\kappa_{mn}^+ M_0 & 0 & 0 & i\kappa_{mn}^+ \\ 0 & i\kappa_{mn}^+ M_0 & 0 & -\dfrac{\alpha_{mn}\mathrm{J}'_m}{\mathrm{J}_m} \\ 0 & 0 & i\kappa_{mn}^+ M_0 & -m\omega_0 \\ i\kappa_{mn}^+ & -\dfrac{1}{r} - \dfrac{1}{\Delta r} & m/\omega_0 & i\kappa_{mn}^+ M_0 \end{bmatrix}}_{\mathrm{A}}$$

$$\times \underbrace{\begin{bmatrix} u'|_{r=1} \\ v'|_{r=1} \\ w'_t|_{r=1} \\ p'|_{r=1} \end{bmatrix}}_{\mathrm{x}} + \underbrace{\begin{bmatrix} 0 \\ 0 \\ 0 \\ \dfrac{1}{\Delta r} \end{bmatrix}}_{\mathrm{B}} \underbrace{[v'|_{1-\Delta r}]}_{\mathrm{u}},$$

$$\underbrace{p'|_{r=1}}_{\mathrm{y}} = \underbrace{[0\,0\,0\,1]}_{\mathrm{C}} \underbrace{\begin{bmatrix} u'|_{r=1} \\ v'|_{r=1} \\ w'_t|_{r=1} \\ p'|_{r=1} \end{bmatrix}}_{\mathrm{x}}. \tag{23}$$

The above time domain state space model is generated by directly reformulating the LEE model [Eqs. (3a)–(3d)] at $r = 1$ and placing all the terms except those derivatives of time to the right-hand sides.[40] It should be noted that ρ_0 and r are normalized to unit values, and $\partial p'/\partial r$ is approximated using the related analytical general solution. Provided $(\mathbf{A}, \mathbf{B}, \mathbf{C})$ we would have $P(s)$ shown in Fig. 3 as $P(s) = \mathbf{C}(s\mathbf{I} - \mathbf{A})^{-1}\mathbf{B}$.

B. Analysis and design methods in control

This control-oriented model enables us to gain an insightful view of time domain impedance boundary conditions from a totally new perspective. In particular, the block diagram of a typical (negative) feedback system in frequency domain is shown in Fig. 3. The transfer function of the overall system is $P(s)/(1 + P(s)F(s))$. The overall system becomes unstable if the magnitude of the loop gain $|P(s)F(s)|$ equals unity and the associated phase of $\angle P(s)F(s)$ approaches $-180°$.

Moreover, the difference between $\angle P(s_1)F(s_1)$ and the $-180°$ line is the so-called phase margin, with s_1 the gain crossover frequency at which $|P(s_1)F(s_1)| = 1$. The phase margin usually represents the proximation of the associated system to instabilities. In this work, numerical disturbances could arise due to the impedance discontinuity between the hard wall and the soft lining wall or could develop through reflections from the outlet boundary. Those numerical disturbances act as perturbations and would make a numerical system unstable if the associated phase margin is insufficient.

The so-called phase-lead compensator could be used to improve the overall phase lead [see Fig. 3(b)]. A phase-lead compensator usually takes the following form:

$$L(s) = \frac{1}{A_{pl}} \frac{1 + aT_a s}{1 + T_a s}, \tag{24}$$

with $[1/aT_a,\ 1/T_a]$ the working bandwidth (i.e., $a > 1$). A larger value of a corresponds to a greater phase lead $\angle L(s)$ which achieves the maximum (up to 90°) at $1/\sqrt{a}T_a$. More details of the phase-lead compensator can be found in any textbook of classical control.[23] The essential concept of this work is to include appropriate phase-lead compensators to construct stable time domain impedance boundary conditions.

IV. STABILITY ANALYSIS

A. Uncompensated impedance boundary conditions

Figure 3(a) shows that $1/Z(s)$ should be stable to ensure the stability of the overall system. First, we analyze the formulation proposed in the literature,[20]

$$\frac{1}{Z(s)} = \begin{cases} s/(\Re s - \mathfrak{X}\omega_0), & \text{if } \mathfrak{X} \leq 0, \\ \omega_0/(\Re\omega_0 + \mathfrak{X}s), & \text{if } \mathfrak{X} > 0. \end{cases} \tag{25}$$

It is easy to confirm that $Z(s) = \Re + i\mathfrak{X}$ at any specified frequency ω_0 by setting $s = i\omega_0$ (which is a common manipulation in signal processing and control). In addition, the poles of the two transfer functions in Eq. (25) are all in the left-half of the s-plane that ensures the so-called BIBO stability. If we adopt the Ingard boundary condition for a steady uniform background mean flow, a direct extension of Eq. (25) yields the corresponding time domain boundary conditions as

$$\frac{\mathrm{d}p'}{\mathrm{d}t} = \Re\frac{\mathrm{d}v'}{\mathrm{d}t} - \mathfrak{X}\omega_0 v' - M_0\frac{\partial p'}{\partial x}, \quad \text{if } \mathfrak{X} \leq 0, \tag{26a}$$

$$\omega_0 p' = \mathfrak{X}\frac{\mathrm{d}v'}{\mathrm{d}t} + \Re\omega_0 v' - \omega_0 M_0\int_0^t \frac{\partial p'}{\partial x}dt, \quad \text{if } \mathfrak{X} > 0, \tag{26b}$$

where the Laplace transform pair between frequency domain and time domain, $s \leftrightarrow \partial/\partial t$, is adopted. In the remaining part of this paper, Eqs. (26a)–(26b) are called the uncompensated impedance boundary conditions, which are unstable for steady uniform background mean flow case, as have been pointed out by Tam and Auriault.[20]

B. Stationary mean flow

In this work, we found that the stability of $1/Z(s)$ alone is not sufficient to ensure the stability of the overall system, even for stationary flow cases. We use Bode plot to explain this issue. A Bode plot consists of magnitude plot and phase plot to show the frequency response of the system. The left panel of Fig. 4 shows the Bode plot of $P(s)$ which is developed from Eq. (23), where $Z = 0.8 \pm i$ and $(m, n) = (4,\ 1)$. The corresponding value of κ_{mn}^+ is achieved by solving Eq. (6) and Eq. (8) together.

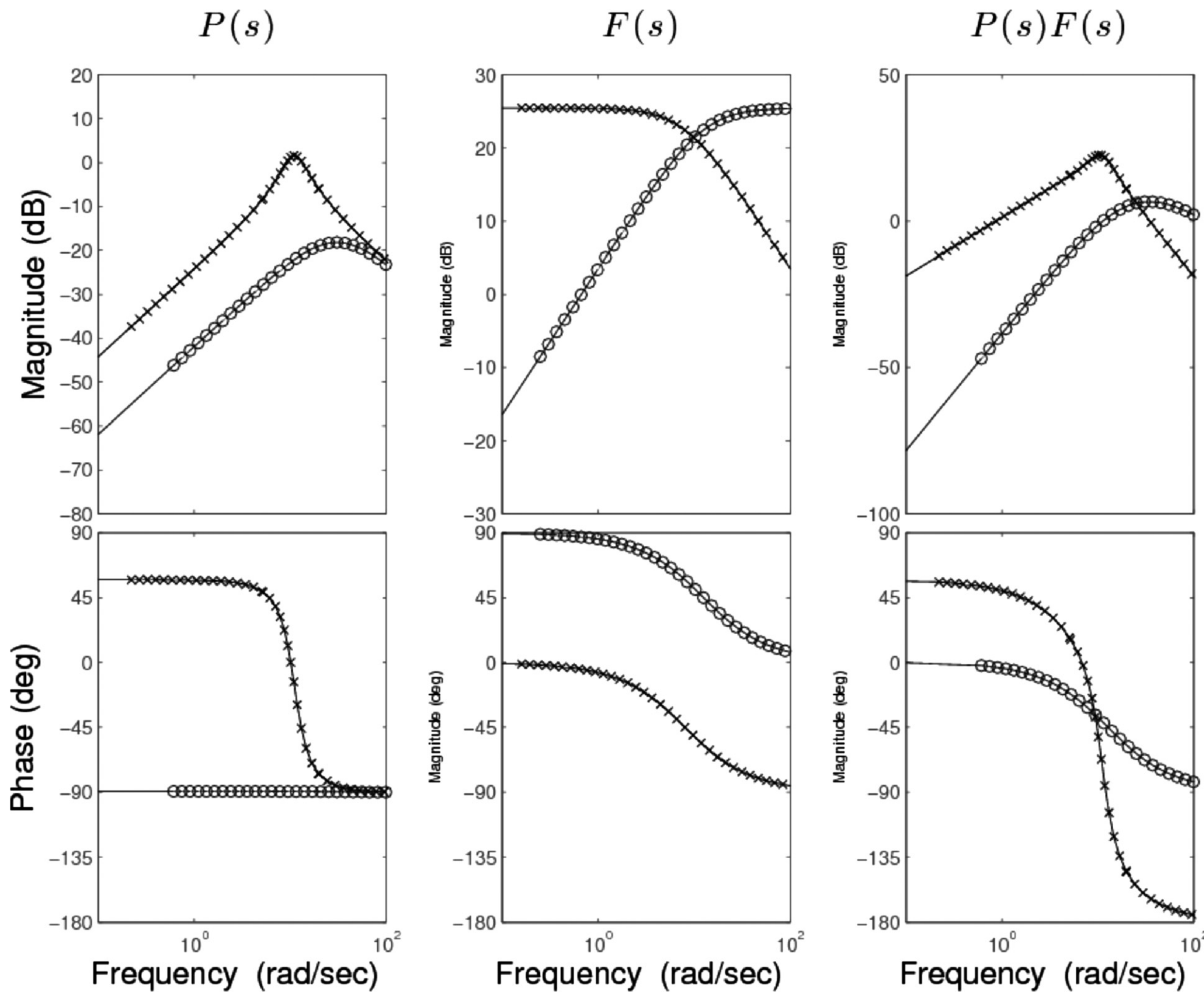

FIG. 4. The Bode plots for the case with $M_0 = 0$ and $Z = 0.8 \pm i$ at $\omega_0 = 10$. The top and bottom panels are magnitude plots and phase plots, respectively. The left panel is for $P(s)$. The middle panel is for the feedback loop, $F(s) = \delta(r-1)/Z(s)$ where $\delta(r-1)$ is approximated with $1/\Delta r$ (Ref. 39). The right panel is for the loop transfer function, $P(s)F(s)$. Here the curves with $(\bigcirc)$ is for the case with $Z = 0.8 - i$, and the curves with $(\times)$ is for $Z = 0.8 + i$. According to Eq. (25), $1/Z(s) = s/(0.8s + 10)$ for $Z = 0.8 - i$, and $1/Z(s) = 10/(s + 8)$ for $Z = 0.8 + i$.

It can be seen that $P(s)$ itself is stable since $|P(s)| = 1$ and $\angle[P(s)] = -180°$ would not be simultaneously satisfied. However, it should be noted that $P(s)$ is a control-oriented model of the original LEE model at $r = 1$ with a couple of simplifications. The stability of $P(s)$ does not necessarily correspond to the stability of the LEE model. A measure usually used to examine the proximity to instability is phase margin. A generally accepted rule of thumb in control practices is to have a phase margin of almost 45°. For this case, the phase margin of $P(s)$ alone is at least 90°. However, the phase margin rapidly decreases if we include the uncompensated impedance boundary condition for the case with $\mathfrak{X} > 0$, because $1/Z(s) = \omega_0/(\Re\omega_0 + \mathfrak{X}s)$ introduces up to 90° phase lag at the high frequency range (see the curve with "$\times$" in the middle panel of Fig. 4). On the other hand, the uncompensated impedance boundary condition for $\mathfrak{X} \leq 0$ would cause no numerical instability since $1/Z(s) = s/(\Re s - \mathfrak{X}\omega_0)$ actually introduces a preferred phase lead up to 90° (see the circled curve in the middle panel of Fig. 4).

The above analysis suggests that the uncompensated impedance boundary condition for $\mathfrak{X} > 0$ would cause numerical instabilities, which will be confirmed by numerical simulations and resolved by the inclusion of a phase compensator in the following sections.

C. Steady uniform background mean mean flow

The adoption of the Ingard boundary condition would introduce an additional transfer function in the form of

$$Ig(s) = \frac{s - iM_0\kappa^+_{mn}}{s} \tag{27}$$

in the feedback loop. It should be noted $Ig(s)$ is an approximation of $Ig(s)$ in Eq. (15). The latter one cannot be directly analyzed using classical control methods due to the existence of a spatial derivative. In particular, by following Eq. (22), we have $I_g \approx (s - \Sigma_{l=0}^{+\infty} iM_0\kappa^+_{ml})/s$ if $A^-_{ml} \ll A^+_{ml}$, $\forall l$. Furthermore, we would achieve Eq. (27) if $A^+_{ml} \ll A^+_{mn}$, $\forall l \neq n$. Here the mode of (m, n) and amplitude A^+_{mn} are related to the incident spinning wave, while the mode of (m, l), A^+_{ml} and A^-_{mn} are related to the reflecting and scattering waves. Analytical solutions of A^+_{ml}/A^+_{mn} and A^+_{ml}/A^+_{mn} can be found in Ref. 31 and are thus omitted here. Generally speaking, the assumptions of

$A^-_{ml}/A^+_{mn} \ll 1$ and $A^+_{ml}/A^+_{mn} \ll 1$ are appropriate and Eq. (27) is thus a reasonable approximation.

Figure 2 implies that κ^+_{mn} will vary along with Z and the phase angle of $Ig(s)$ will change accordingly. As an example, if we set $Z = 0.8 \pm i$ at $\omega_0 = 10$, the corresponding Bode plot of $Ig(s)$ is shown in the middle panel of Fig. 5, which suggests that the Ingard boundary condition would cause huge phase lag, up to 90° for the $\mathfrak{X} < 0$ case and up to almost 180° for the $\mathfrak{X} > 0$ case, both at the low frequency range. The overall loop transfer function is shown in the right panel of Fig. 5, where $(m, n) = (4, 1)$. It can be seen that the unstable points at low frequencies (where the frequency $<\omega_0$) is caused by the inclusion of the Ingard boundary condition, and the instability at high frequencies (where the frequency $>\omega_0$) is caused by $Z(s)$ itself. For $\mathfrak{X} < 0$ case, the phase margin of the entire close-loop system becomes quite poor at the low frequency range. On the other hand, for $\mathfrak{X} > 0$ case, the phase margin of the overall system will become insufficient at both the low and high frequency ranges. The above analysis predicts that the uncompensated impedance boundary conditions for both $\mathfrak{X} > 0$ and $\mathfrak{X} < 0$ cases will cause numerical instabilities in a steady uniform background mean flow. This prediction will be numerically confirmed and a solution of the issue will be given in the following sections.

V. COMPENSATED IMPEDANCE BOUNDARY CONDITION DESIGN

For stationary flow cases with $\mathfrak{X} > 0$, the above analysis (see Fig. 4) shows that numerical instabilities would arise at the high frequency range, where the corresponding phase margin of the overall system approaches zero. To resolve this stability issue, here we include a phase-lead compensator in the form of Eq. (10) to provide a phase-lead compensation of up to 90° within the frequency range between $1/(aT_a)$ and $1/T_a$. The suggested parameters of this phase-

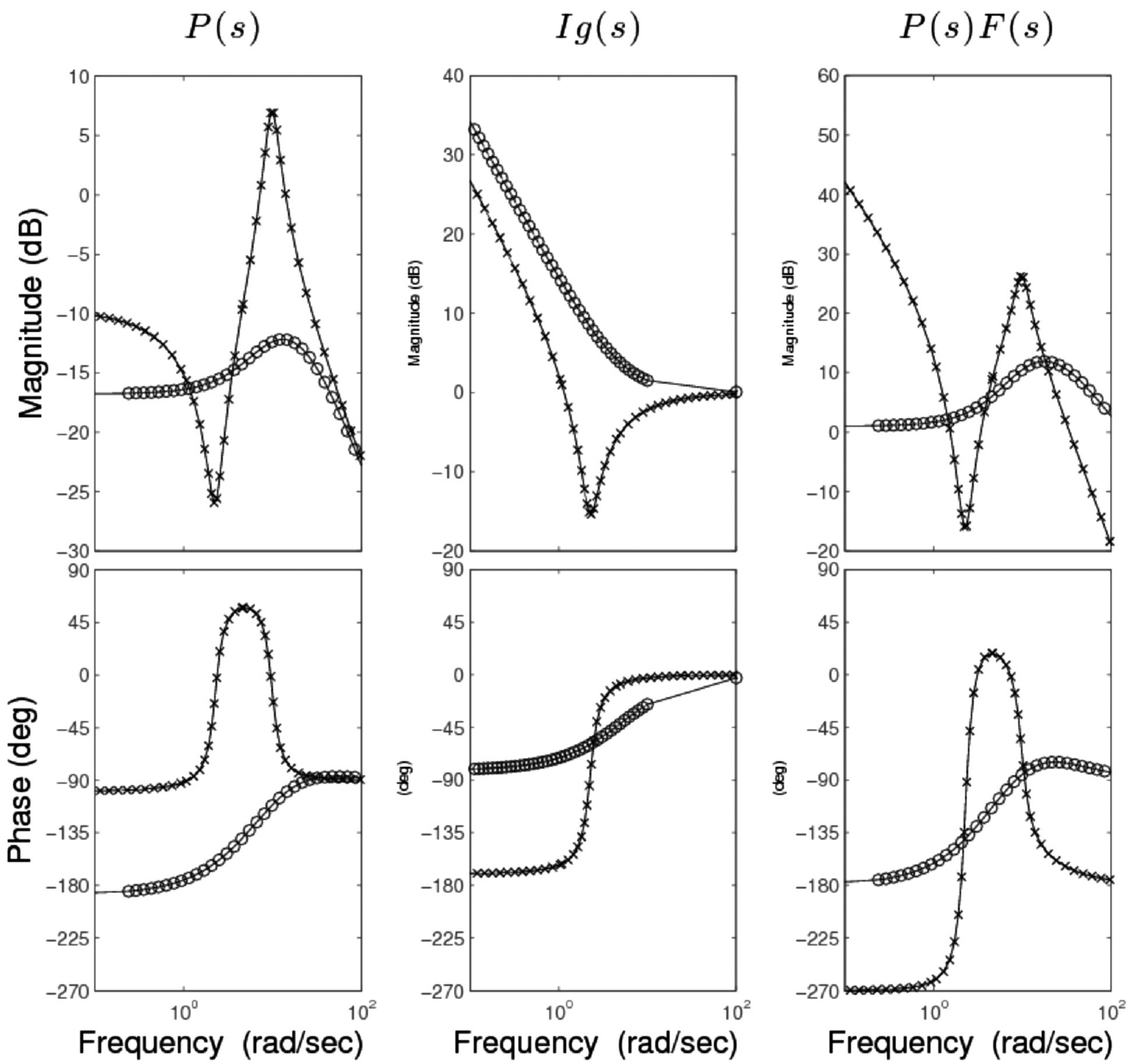

FIG. 5. The Bode plots for the case with $M_0 = 0.3$ and $Z = 0.8 \pm i$. The left panel is for $P(s)$. The middle panel is for the corresponding Ingard boundary condition, $Ig(s)$. The right panel is for the associated loop transfer function, $P(s)F(s) = P(s)\,Ig(s)\delta(r-1)/Z(s)$, where $\delta(r-1)$ is approximated with $1/\Delta r$ (Ref. 39). Here the curves with (○) is for the case with $Z = 0.8 - i$, and the curves with (×) is for $Z = 0.8 + i$.

lead compensator [Eq. (10)] will ensure $|L(s)| \approx 1$ and $\angle L(s) \approx 0$ with $s = i\omega_0$, where ω_0 is the frequency of incident sound wave. In other words, the performance of the impedance at the desired frequency ω_0 will remain almost intact by the inclusion of this compensator. Then, we achieve the following compensated impedance boundary condition:

$$\frac{\hat{v}'}{\hat{p}'} = \underbrace{\frac{(1/s + aT_a)}{(1/s + T)} \frac{1}{A_{pl}}}_{L_a(s)} \underbrace{\frac{\omega_0}{(\Re\omega_0 + \mathfrak{X}s)}}_{Z(s)}, \text{ if } \mathfrak{X} > 0 \text{ and } M_0 = 0. \tag{28}$$

It would be a matter of straight algebra to achieve the corresponding time domain impedance boundary condition [as Eq. (12)]. Here, s and $1/s$ in frequency domain correspond to d/dt and $\int_0^t$ in time domain, respectively.

For steady uniform background mean flow cases with $\mathfrak{X} < 0$, another phase-lead compensator can be included in the feedback loop to provide an additional phase-lead at low frequency ranges,

$$\frac{\hat{v}'}{\hat{p}'} = \underbrace{\frac{s + M_0(\partial/\partial x)}{s}}_{I_g(s)} \underbrace{\left(\frac{T_b s}{T_b s + 1}\right)^b}_{L_b(s)} \underbrace{\frac{s}{(\Re s - \mathfrak{X}\omega_0)}}_{Z(s)}, \tag{29}$$

where b is set to 2. As a result, $L_b(s)$ will introduce a phase lead up to 180° at the low frequency range smaller than $1/T_b$ that should be larger than $|M_0\kappa^+|$, which is almost unity for most spinning mode cases with $M_0 \leq 0.3$. Then, T_b is simply set to unity in this design. To generate the corresponding time domain impedance boundary condition from Eq. (29), we adopt the following Laplace transform pairs between frequency domain and time domain: $s \leftrightarrow \partial/\partial t$ and $s^2 \leftrightarrow -\omega_0^2$. The latter simplification enables us to avoid high-order time derivatives. Then, the aforementioned time domain impedance boundary condition, Eq. (16), can be achieved.

Finally, for steady uniform background mean flow cases with $\mathfrak{X} > 0$, we include two phase-lead compensators to compensate phase lags at low and high frequency ranges, respectively. The transfer function becomes

$$\frac{\hat{v}'}{\hat{p}'} = \underbrace{\frac{(1 + aT_a s)}{(1 + T_a s)} \frac{1}{A_{pl}}}_{L_a(s)} \underbrace{\left(\frac{T_b s}{T_b s + 1}\right)^b}_{L_b(s)} \underbrace{\frac{s + M_0(\partial/\partial x)}{s}}_{Ig(s)} \times \underbrace{\frac{\omega_0}{(\Re\omega_0 + \mathfrak{X}s)}}_{Z(s)}. \tag{30}$$

Again, $b = 2$ and $T_b = 1$. After some straightforward algebra, the corresponding time domain boundary condition [as Eq. (17)] can be achieved. It should be noted that the approximate form $Ig(s) = (s - M_0\kappa_{mn}^+)/s$ is used in the above stability analysis, whereas the exact form $Ig(s) = (s + M_0\partial/\partial x)/s$ is used here to construct the time domain impedance boundary conditions.

In summary, here we include two phase-lead compensators, $L_a(s)$ and $L_b(s)$, to compensate phase lags at the high and low frequency ranges, respectively. The compensators are carefully designed to ensure that the frequency response at the tonal frequency ω_0 of the incident wave remains almost intact, i.e., $|L_a(i\omega_0)| \approx 1$, $|L_b(i\omega_0)| \approx 1$, $\angle L_a(i\omega_0) \approx 0°$, and $\angle L_b(i\omega_0) \approx 0°$. Otherwise, a numerical simulation with the compensated impedance boundary conditions would produce stable results, which, however, correspond to incorrect impedance at ω_0. The assumption implicitly made here is that the phase margin of the entire numerical system at ω_0 should be satisfactory. This assumption can be assured by a close examination of Eq. (25) and Eq. (27), which cause the phase lags that are however negligible at ω_0.

VI. RESULTS AND DISCUSSION

Here we study the aforementioned time domain impedance boundary conditions using the computational set-up as shown in Fig. 1. According to the literature,[3] the normalized values of $Z(i\omega)$ are chosen within the range of $0.5 < \Re < 1.5$ and $-1.5 \leq \mathfrak{X} \leq 1.5$.

Figure 6 shows the computational results for a typical case of $(m, n) = (4, 1)$ with $\omega_0 = 10$ and $Z = 1 + i$. We first use the uncompensated time domain impedance boundary conditions [Eqs. (26a)–(26b)]. It can be seen that numerical instabilities developing from the hard-soft interface at $(x, r) = (0, 1)$ will quickly overwhelm the right-directing incident sound wave. In addition, the numerical instabilities may consist of both short wavelength and long wavelength waves compared to the wavelength of the incident sound wave.

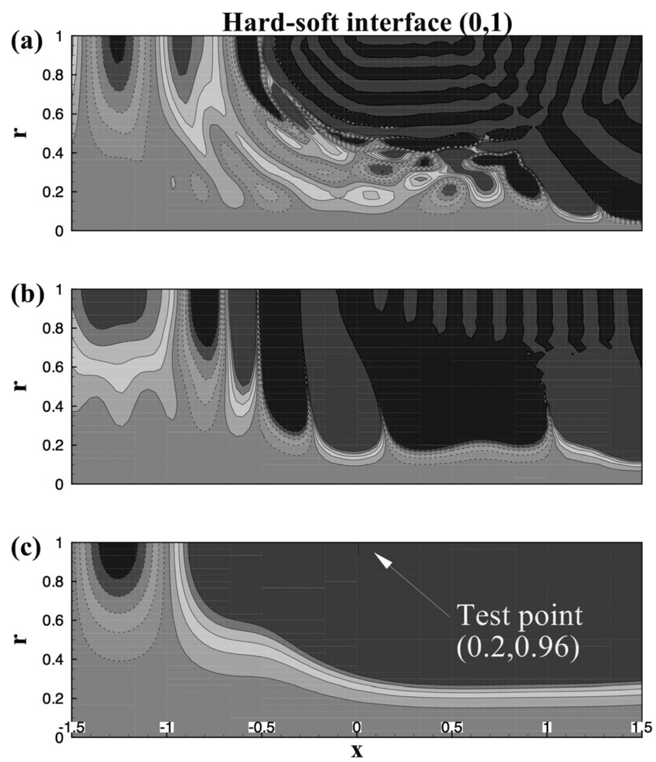

FIG. 6. The instantaneous near-field modal sound pressure field using unstable lining impedance boundary conditions. Here the spinning mode is $(m, n) = (4, 1)$ at $\omega_0 = 10$, and (a) $M_0 = 0$, $Z = 0.8 + i$; (b) $M_0 = 0.3$, $Z = 0.8 + i$; and (c) $M_0 = 0.3$, $Z = 0.8 - i$. This figure is displayed with 10 contour levels between $\pm 10^{-4}$.

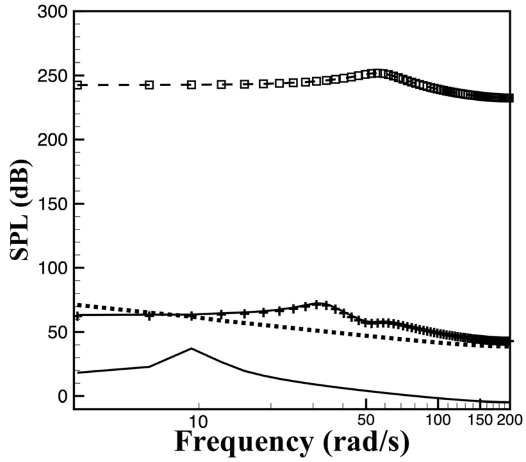

FIG. 7. Spectrum of the time series measured at the test point $(x, r) = (0.2, 0.96)$ for the cases in Fig. 6. The curves from top to bottom are $(\square) : M_0 = 0,\ Z = 0.8 + i$; $(+) : M_0 = 0.3,\ Z = 0.8 + i$; $(\cdots) : M_0 = 0.3,\ Z = 0.8 - i$; and $(-)$ the spectrum of the incident spinning modal wave.

To further quantitate the instabilities, the time series of one measurement point at $(x, r) = (0.2, 0.96)$ are recorded for each case to generate the associated spectrum using fast Fourier transform. The resultant spectrum is shown in Fig. 7. It can be seen that the spectrum of a correct simulation should have a peak at $\omega_0 = 10$ with sound pressure level (SPL) of almost 34 dB. In contrast, the uncompensated lining impedance boundary conditions, Eqs. (26a)–(26b), would lead to numerical instabilities: (1) For $\mathfrak{X} > 0$ at $M_0 = 0$, the overall numerical system has a very poor phase margin at the high frequency range (see the curve with $\times$ in the right panel of Fig. 4), where the numerical instability would appear. This analytical outcome is supported here by the corresponding spectrum (the curve with the symbol $\square$ in Fig. 7) that has a peak at a very high frequency of almost 60 rad/s with numerically unstable SPL of more than 250 dB; (2) For $\mathfrak{X} > 0$ and $M_0 = 0.3$, the previous stability analysis (see the curve with $\times$ in the right panel of Fig. 5) shows that the unstable frequency would be possibly lower than the former case. This prediction can be supported here as well (see the curve with the symbol $+$ in Fig. 7); (3) For $\mathfrak{X} < 0$ and $M_0 = 0.3$, the previous stability analysis (see the curve with $\times$ in the right panel of Fig. 5) suggests that the overall system would become unstable at a very low frequency. The spectrum result (see the dotted curve in Fig. 7) confirms this analysis as well. In summary, Figs. 6 and 7 show that the uncompensated lining impedance boundary conditions lead to numerical instabilities and the resultant numerical nuisance can be analyzed and predicted using the analytical approach developed in this work.

Next, we validate the compensated lining impedance boundary conditions developed in this work. Figure 8 shows the computational results for the case with an impedance of $\mathfrak{X} > 0$ at $M_0 = 0$ using the corresponding compensated boundary condition, Eq. (12). The numerical results are compared to the asymptotic solutions achieved by the Wiener-Hopf method. It can be seen that the proposed boundary condition is stable and successfully produces results that agree largely well with the asymptotic solutions in terms of the instantaneous sound pressure and the time-averaged sound pressure fields. In addition, Fig. 9 shows the results for steady uniform background flow case. The results show that the proposed impedance boundary condition, Eq. (17), is stable and successfully produces results comparable to asymptotic solutions for the steady uniform background mean flow case.

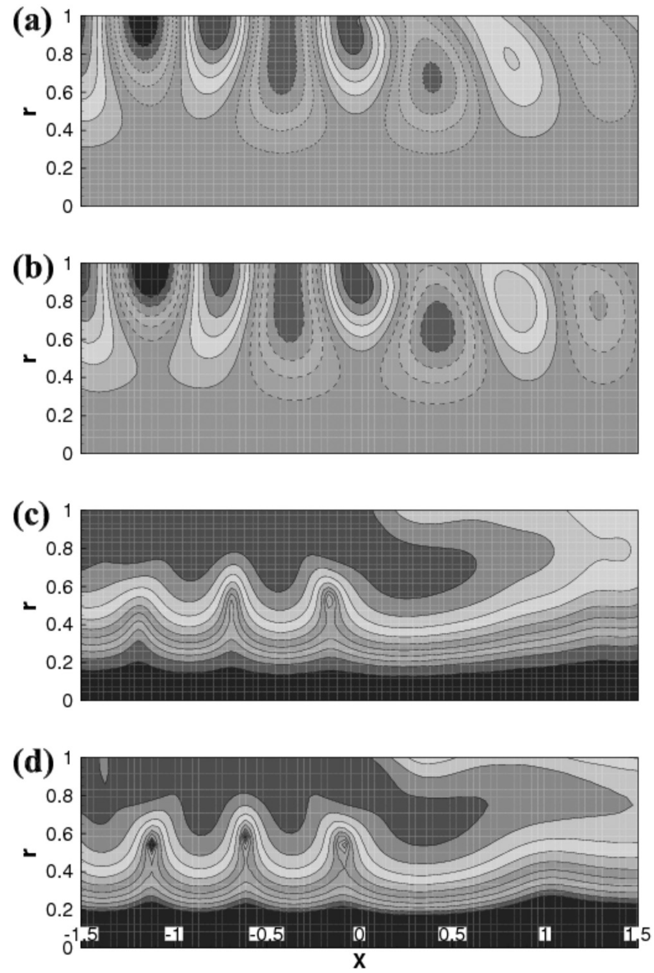

FIG. 8. The near-field sound pressure fields of $(m, n) = (4, 1)$ at $M_0 = 0$, $\omega_0 = 10$. The impedance is $Z = 0.8 + i$, which is implemented using Eq. (12), where (a) and (c) show time domain numerical results with the LEE model and (b and d) the asymptotic solutions using the Wiener-Hopf method, and (a)–(b) are instantaneous sound pressure field, displayed with 10 contour levels between $\pm 10^{-4}$ and (c)–(d) are time-averaged sound pressure field, displayed with 10 contour levels from -20 to 0 dB.

It should be noted that the sound pressure patterns between the numerical and asymptotic results are slightly different in Figs. 8 and 9. One potential reason is that the asymptotic solution is achieved by performing inverse Fourier transformation and a limited integral range has to be used for the associated numerical integration.

More validation results can be found in Table I. To quantitate the proposed boundary conditions, the difference between the transmission losses, $TL_{LEE} - TL_{WH}$, is examined, where TL_{LEE} denotes the transmission loss calculated by the time domain LEE solver and TL_{WH} denotes the transmission loss calculated by the Wiener-Hopf method. Here the transmission loss is evaluated by calculating the time-averaged difference of acoustic power between $x = -0.5$ and $x = 0.5$. It can be seen that the largest difference is less

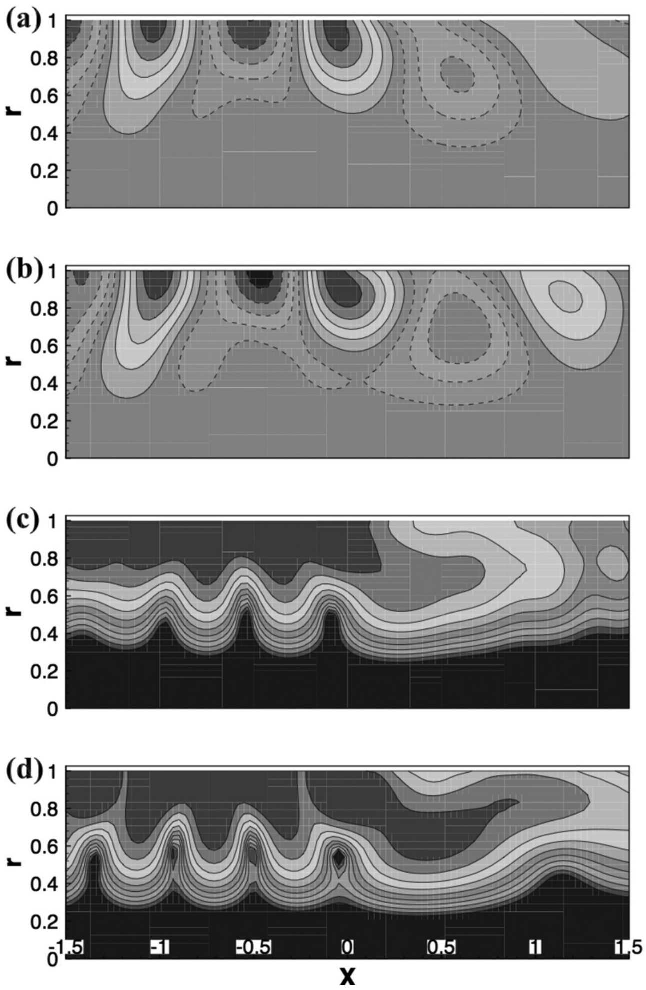

FIG. 9. The near-field sound pressure fields of $(m, n) = (4, 1)$ at $M_0 = 0.3$, $\omega_0 = 10$. The impedance is $Z = 0.8 + i$, which is implemented using Eq. (17). The other set-ups and display styles are the same as those in Fig. 8.

than 1.17 dB and the difference of more than half the cases is less than 0.5 dB, evidencing the performance of the proposed compensated boundary conditions are consistently good. Exhaustive validations have been performed for much more cases and similar conclusions can be made.

It is worthwhile to mention that the proposed design method has also been successfully applied to a generic bypass duct case in the presence of a mean flow field with an infinitely thin boundary layer. The Myers boundary condition was used to take account of the slow varying curvature of the duct. It is straightforward to extend the code, and more results are omitted here for brevity of the current paper.

VII. SUMMARY

A series of the so-called compensated impedance boundary conditions have been developed in this work from the perspective of control. In particular, the proposed control-oriented model shown in Fig. 3 and the phase-lead compensator based design strategy used in Eqs. (9)–(17) are the most innovative and important results of this work. Using these equations and modeling concepts, we are able to analyze numerical stability of various impedance boundary conditions, design new impedance boundary conditions, and finally perform stable numerical simulations in time domain for tonal spinning modal sound propagations in a lined duct, with either a stationary or steady uniform background mean flow. The prohibitive computational cost for those modified Ingard-Myers boundary conditions with a thin boundary layer of finite thickness can be saved. The whole design strategy based on the concept of phase compensator in classical control is mathematically clear with little empirical set-ups and generic to various test cases. As a result, the proposed boundary conditions provide an attractive alternative for numerical simulations with liners.

The proposed control-oriented model shows that a lining impedance behaves as a negative feedback to the original sound propagation system. A deep insight of previous work focusing on either the modified Ingard-Myers boundary conditions[16–18] or the numerical schemes[20–22,24–26] could, then, be gained from the perspective of control. Numerical instability, either Kelvin-Helmholtz type[20] or Tollmien-Schlichting type,[21] arises in time domain simulations can be

TABLE I. The difference of the transmission loss between the numerical results with the LEE model and the asymptotic solutions using the Wiener-Hopf method.

Mode m	mode n	ω_0	Mach	Z	$TL_{LEE} - TL_{WH}$
4	1	20	0.2	1-2i	0.26686
4	1	20	0.2	1-1.5i	0.3989
4	1	20	0.2	1-i	0.5055
4	1	20	0.2	1-0.5i	0.3776
4	1	20	0.2	1	0.1082
4	1	20	0.2	1 + 0.5i	−0.0325
4	1	20	0.2	1 + i	−0.4
4	1	20	0.2	1 + 1.5i	−1.603
4	1	15	0	1 + 0.5i	0.1192
4	1	15	0.1	1 + 0.5i	0.3952
4	1	15	0.2	1 + 0.5i	0.439
4	1	15	0.3	1 + 0.5i	0.7341
4	2	25	0.1	1 + 1.5i	0.24274
4	2	25	0.1	1.1 + 1.5i	0.24472
4	2	25	0.1	1.3 + 1.5i	0.24701
4	2	25	0.1	1.5 + 1.5i	0.2203
9	1	20	0	1 + i	0.5464
9	1	20	0	1 − i	0.2682
9	1	20	0.1	1 + i	0.8465
9	1	20	0.1	1 − i	0.5064
9	1	20	0.2	1 + i	0.908
9	1	20	0.2	1 − i	0.401
9	2	20	0	1 + i	0.2905
9	2	20	0	1 + i	0.0614
9	2	20	0.1	1 + i	0.3777
9	2	20	0.1	1 + i	−0.0069
9	2	20	0.2	1 + i	0.417
9	2	20	0.2	1 + i	−0.0335
13	1	20	0	1 − 2i	0.7857
13	1	20	0	1 − 1.5i	1.0786
13	1	20	0	1 − i	0.934
13	1	20	0	1 − 0.5i	0.7245
13	1	20	0.2	1 − 2i	−1.0835
13	1	20	0.2	1 − 1.5i	−0.8043
13	1	20	0.2	1 − i	0.78
13	1	20	0.2	1 − 0.5i	1.5724

analyzed by examining dynamic system stability of the corresponding control-oriented model. Our work shows that the development of a stable time domain impedance boundary condition is equivalent to a stabilized controller design.

Last but not least, the lined duct acoustic application studied in this work would also provide new academic problems to the further development of control theory. For example, the associated transfer functions include complex-valued parameters (see Fig. 3) and might be irrational. Such features are unordinary for control theory, not to mention the non-minimum phase behavior of the feedback loop. All these issues call for further theoretical investigations.

ACKNOWLEDGMENT

This work was supported by National Natural Science Foundation of China (grants 11172007 and 11322222) and Commercial Aircraft Engine Co., Ltd., China.

[1]B. J. Tester, "Some aspects of sound attenuation in lined ducts containing inviscid mean flows with boundary layers," J. Sound Vib. **28**, 217–245 (1973).
[2]J. M. G. S. Oliveira and P. J. S. Gil, "Sound propagation in acoustically lined elliptical ducts," J. Sound Vib. **333**, 3743–3758 (2013).
[3]J. Yu, M. Ruiz, and H. W. Kwan, "Validation of Goodrich perforate liner impedance model using NASA Langley test data," AIAA Paper 2008–2930 (2008).
[4]C. Bogey, C. Bailly, and D. Juvé, "Computation of flow noise using source terms in linearized Euler's equations," AIAA J. **40**, 235–243 (2002).
[5]C. Richter, F. H. Thiele, X. Li, and M. Zhuang, "Comparison of time-domain impedance boundary conditions for lined duct flows," AIAA J. **45**, 1333–1345 (2007).
[6]X. Huang, X. Zhang, and S. K. Richards, "Adaptive mesh refinement computation of acoustic radiation from an engine intake," Aerosp. Sci. Technol. **12**, 418–426 (2008).
[7]D. Casalino and M. Genito, "Turbofan aft noise predictions based on Lilley's wave model," AIAA J. **46**, 84–93 (2008).
[8]S. W. Rienstra, "Acoustic scattering at a hard-soft lining transition in a flow duct," J. Eng. Math. **59**, 451–475 (2007).
[9]E. J. Brambley, "Well-posed boundary condition for acoustic liners in straight ducts with flow," AIAA J. **49**, 1272–1282 (2011).
[10]C. K. W. Tam and J. C. Webb, "Dispersion-relation-preserving finite difference schemes for computational acoustics," J. Comput. Phys. **107**, 262–281 (1993).
[11]X. Huang, X. X. Chen, Z. K. Ma, and X. Zhang, "Efficient computation of spinning modal radiation through an engine bypass duct," AIAA J. **46**, 1413–1423 (2008).
[12]A. Agarwal, P. J. Morris, and R. Mani, "Calculation of sound propagation in nonuniform flows: suppression of instability waves," AIAA J. **42**, 80–88 (2004).
[13]U. Ingard, "Influence of fluid motion past a plane boundary on sound reflection, absorption, and transmission," J. Acoust. Soc. Am. **31**, 1035–1036 (1959).
[14]M. K. Myers, "On the acoustic boundary condition in the presence of flow," J. Sound Vib. **71**, 429–434 (1980).
[15]W. Eversman and R. J. Beckemeyer, "Transmission of sound in ducts with thin shear layers: Convergence to the uniform flow case," J. Acoust. Soc. Am. **52**, 216–220 (1972).
[16]E. J. Brambley, "Fundamental problems with the model of uniform flow over acoustic linings," J. Sound Vib. **322**, 1026–1037 (2009).
[17]Y. Renou and Y. Auregan, "Failure of the Ingard-Myers boundary condition for a lined duct: An experimental investigation," J. Acoust. Soc. Am. **130**, 52–60 (2011).
[18]S. W. Rienstra and M. Darau, "Boundary layer thickness effects of the hydrodynamic instability along an impedance wall," J. Fluid Mech. **671**, 559–573 (2011).
[19]G. Gabard, "A comparison of impedance boundary conditions for flow acoustics," J. Sound Vib. **332**, 714–724 (2013).
[20]C. K. W. Tam and L. Auriault, "Time-domain impedance boundary conditions for computational aeroacoustics," AIAA J. **34**, 917–923 (1996).
[21]X. D. Li, C. Richter, and F. Thiele, "Time-domain impedance boundary conditions for surfaces with subsonic mean flows," J. Acoust. Soc. Am. **119**, 2655–2676 (2006).
[22]Y. Özyörük and L. N. Long, "Time-domain numerical simulation of a flow-impedance tube," J. Comput. Phys. **146**, 29–57 (1998).
[23]S. Eduardo, *Mathematical Control Theory: Deterministic Finite Dimensional Systems*, 2nd ed. (Springer, Berlin, Germany, 1998).
[24]K. Y. Fung, H. B. Ju, and B. Tallapragada, "Impedance and its time-domain extensions," AIAA J. **38**, 30–38 (2000).
[25]K. Y. Fung and H. B. Ju, "Broadband time-domain impedance models," AIAA J. **39**, 1449–1454 (2001).
[26]H. B. Ju and K. Y. Fung, "Time-domain impedance boundary conditions with mean flow effects," AIAA J. **39**, 1683–1690 (2001).
[27]C. Richter, P. L. Hay, and J. A. N. Schönwald, "A review of time-domain impedance modelling and applications," J. Sound Vib. **330**, 3859–3873 (2011).
[28]Y. Özyörük and V. Ahuja, "Numerical simulation of fore and aft sound field of a turbofan," AIAA J. **42**, 2028–2034 (2004).
[29]R. M. Munt, "The interaction of sound with a subsonic jet issuing from a semi-infinite cylindrical pipe," J. Fluid Mech. **83**, 609–640 (1977).
[30]S. W. Rienstra, "Acoustic radiation from a semi-infinite annular duct in a uniform subsonic mean flow," J. Sound Vib. **94**, 267–288 (1984).
[31]G. Gabard and R. J. Astley, "Theoretical model for sound radiation from annular jet pipes: Far- and near-field solutions," J. Fluid Mech. **549**, 315–341 (2006).
[32]X. Zhang, X. X. Chen, C. L. Morfey, and P. A. Nelson, "Computation of spinning modal radiation from an unflanged duct," AIAA J. **42**, 1795–1801 (2004).
[33]X. Zhang, X. X. Chen, and C. L. Morfey, "Acoustic radiation from a semi-infinite duct with a subsonic jet," Int. J. Aeroacoustics **4**, 169–184 (2005).
[34]E. Peers and X. Huang, "High-order schemes for predicting computational aeroacoustic propagation with adaptive mesh refinement," Acta. Mech. Sin. **29**, 1–11 (2013).
[35]F. Q. Hu, M. Y. Hussaini, and J. Manthey, "Low-dissipation and low-dispersion Runge-Kutta schemes for computational acoustics," J. Comput. Phys. **124**, 177–191 (1996).
[36]G. Ashcroft and X. Zhang, "Optimized prefactored compact schemes," J. Comput. Phys. **190**, 459–477 (2003).
[37]J. Ray, C. A. Kennedy, S. Lefantzi, and H. N. Najm, "Using high-order methods on adaptively refined block-structured meshes—Derivatives, interpolations, and filters," SIAM. J. Sci. Comput. **29**, 139–181 (2007).
[38]S. K. Richards, X. X. Chen, X. Huang, and X. Zhang, "Computation of fan noise radiation through an engine exhaust geometry with flow," Int. J. Aeroacoustics **6**, 223–241 (2007).
[39]X. Huang and X. Zhang, "The Fourier pseudospectral time-domain method for some computational aeroacoustics problems," Int. J. Aeroacoustics **5**, 279–294 (2006).
[40]Q. K. Wei, X. Huang, and E. Peers, "Acoustic imaging of a duct spinning mode by the use of an in-duct circular microphone array," J. Acoust. Soc. Am. **133**, 3986–3994 (2013).